



Defect and void evolution in oxide dispersion strengthened ferritic steels under 3.2 MeV Fe⁺ ion irradiation with simultaneous helium injection

I.-S. Kim^a, J.D. Hunn^b, N. Hashimoto^b, D.L. Larson^{b,1}, P.J. Maziasz^b,
K. Miyahara^a, E.H. Lee^{b,*}

^a Department of Molecular Design and Engineering, Nagoya University, Nagoya, Japan

^b Metals and Ceramics Division, Oak Ridge National Laboratory, Oak Ridge, P.O. Box 2008, TN 37831-6376, USA

Received 8 December 1999; accepted 27 April 2000

Abstract

In an attempt to explore the potential of oxide dispersion strengthened (ODS) ferritic steels for fission and fusion structural materials applications, a set of ODS steels with varying oxide particle dispersion were irradiated at 650°C, using 3.2 MeV Fe⁺ and 330 keV He⁺ ions simultaneously. The void formation mechanisms in these ODS steels were studied by juxtaposing the response of a 9Cr–2WVTa ferritic/martensitic steel and solution annealed AISI 316LN austenitic stainless steel under the same irradiation conditions. The results showed that void formation was suppressed progressively by introducing and retaining a higher dislocation density and finer precipitate particles. Theoretical analyses suggest that the delayed onset of void formation in ODS steels stems from the enhanced point defect recombination in the high density dislocation microstructure, lower dislocation bias due to oxide particle pinning, and a very fine dispersion of helium bubbles caused by trapping helium atoms at the particle–matrix interfaces. © 2000 Elsevier Science B.V. All rights reserved.

PACS: 81.20.Ev; 81.30.Mh; 61.80.Jh; 61.70.Yq

1. Introduction

In recent years, oxide dispersion strengthened (ODS) ferritic steels have been considered for structural materials for advanced fast breeder reactors and future fusion first wall applications [1–3]. These efforts are motivated mainly by the fact that ODS steels have superior creep resistance which permits operation at higher temperatures [1–4], and they have outstanding stability under irradiation [5], and meet low activation criteria for fu-

sion power system [3]. In a 4 MeV Ni ion irradiated 12Cr–8Mo–0.1Y₂O₃ ODS ferritic steel, no voids were found after irradiation up to 300 dpa with 4 MeV Ni³⁺ ions at 525°C, and it was alluded that the void suppression might be prolonged indefinitely in such an ODS steel without considering the effect of helium generation under neutron irradiation [5]. On the other hand, electron irradiation of a 13Cr–0.23Y₂O₃ steel at 400°C produced a high number density of dislocation loops and faceted voids at oxide particle–matrix interfaces, but void formation was suppressed with increasing irradiation temperature, and ceased at 550°C [4].

In general, ferritic/martensitic steels have shown excellent swelling resistance under both neutron [6–10] and ion irradiation [5,11,12]. It is, however, well known that voids do form in ferritic steels under gas generating environments such as in neutron irradiation [6–10] or ion irradiation with helium injection [11,12]. Although

* Corresponding author. Tel.: +1-865 574 5058; fax: +1-865 574 0641.

E-mail address: leeh@ornl.gov (E.H. Lee).

¹ Present address: Seagate Recording Heads, Mailstop NRWTRI, 7801 Computer Avenue South, Minneapolis, MN 55435-5489, USA.

bias-driven void growth [13] is generally delayed in ferritic steel, evidences suggest that the void growth rate is not much slower than that in austenitic stainless steels once a bias-driven void growth regime is established [14,15].

It is the aim of this paper to elucidate the nature of swelling resistance of ferritic steels and the potential benefit for the inclusion of Y_2O_3 particles in ODS steel. For this study, a set of ODS steels were irradiated together with a tempered martensitic steel, 9Cr–2WVTa, and a solution annealed AISI 316LN austenitic stainless steel under the same irradiation condition by employing 3.2 MeV Fe^+ and 330 keV He^+ ion beams simultaneously. After irradiation, the damage and cavity microstructures were studied with transmission electron microscopy (TEM). The results are explained first by establishing a strong correlation between microstructure and void formation behavior and then analyzing the information under a powerful theoretical framework based on a rate theory model [13].

2. Experimental

The three ODS steels (17Y3, 12Y1, 12YWT) investigated in this work were provided by Kobe Specialty Tube Company in Japan, and the 9Cr–2WVTa ferritic/martensitic steel (Heat #3791) and AISI 316LN austenitic stainless steel (Heat #18474) were procured by Oak Ridge National Laboratory. The alloy compositions are tabulated in Table 1.

The ODS steels were prepared by a mechanical alloying (MA) process, which involved a preparation of pre-alloyed powder of $\approx 70 \mu m$ diameter particle size via an Ar gas atomization process, mixing the metal powder with $\approx 20 \text{ nm } Y_2O_3$ powder in Ar gas atmosphere, milling with high energy attrition type balls for 48 h, degassing for 2 h at $400^\circ C$ in $< 2 \times 10^{-2} \text{ Pa}$ vacuum, hot isostatic press (HIP) canning, hot extrusion to a bar at $1150^\circ C$, hot rolling into plate at $1150^\circ C$, thickness reduction with cold rolling for 17Y3 and 12Y1

and warm rolling at $600^\circ C$ for 12YWT, final annealing at $1050^\circ C$ for 1 h, and air cooling. The detailed alloy preparation procedures can be found in [16]. The 9Cr–2WVTa alloy was prepared by austenitizing at $1050^\circ C$ for 30 min under flowing He, fast inert gas cooling, tempering at $750^\circ C$ for 1 h, and fast inert gas cooling. The AISI 316LN steel was solution annealed at $1050^\circ C$ for 30 min in vacuum.

TEM disks were prepared from each steel by mechanically polishing followed by electrochemical polishing prior to irradiation. Irradiation was carried out with 3.2 MeV Fe^+ and 330 keV He^+ ion beams simultaneously using the Triple Ion Facility (TIF) at ORNL. Details of the triple ion beam facility can be found in [17]. The ion energies were chosen to render the maximum damage and gas atom deposition near a depth of 750–800 nm determined by the computer code, stopping and range of ions in matter (SRIM, 1998 version) [18]. An Fe^+ ion beam was applied to give a peak damage rate of $\approx 10^{-3} \text{ dpa/s}$ (displacements per atom/s) together with $\approx 5 \text{ appm He/dpa}$ injection rate at $650^\circ C$. The final dose attained was 50 dpa with 260 appm He at the peak damage region. The procedure for the dpa calculation is described in [19].

TEM specimens were prepared by electrochemically removing $\approx 700 \text{ nm}$ from the ion bombarded side and then thinning from the unirradiated side until perforation occurred. This procedure produced TEM foils with thicknesses of $\approx 100 \text{ nm}$ on average and allowed examination of the microstructure between 700 and 800 nm original depth. Damage microstructure was examined with JEOL FX2000 and Philips CM30 electron microscopes operated at 200 keV.

The nature of the oxide particles after MA were characterized by an energy-compensated 3-dimensional atom probe field ion microscopy (APFIM). The detailed APFIM study results are published in a separate paper [20]. Here, only brief experimental findings are included in Section 4 to aid the understanding of the state of oxide particle dispersion in the mechanically alloyed ODS steels and its impact on void formation during irradiation.

Table 1
Alloy compositions in wt%^a

Alloy	Fe	Cr	Ni	Mn	Mo	W	V	Ta	Ti	Si	C	P	Y_2O_3
316 LN	Bal	16.31	10.20	1.75	2.07	– ^b	–	–	–	0.39	0.009	0.029	–
9Cr– 2WVTa	Bal	8.72	–	0.43	–	2.09	0.23	0.075	–	0.23	0.10	0.015	–
17Y3	Bal	17.07	–	< 0.1	–	–	–	–	–	< 0.1	< 0.05	< 0.01	0.239
12Y1	Bal	12.35	–	< 0.1	–	–	–	–	–	< 0.1	< 0.05	< 0.01	0.248
12YWT	Bal	12.29	–	< 0.1	–	–	–	–	0.39	< 0.1	< 0.05	< 0.01	0.249

^a Trace inclusions such as B, Co, Ni, Cu, N, S (< 0.01) etc., exist also.

^b Not added.

3. Results

The initial microstructure of solution annealed AISI 316LN austenitic stainless steel was characterized by well defined, clean grains with a very low density of dislocations ($\ll 10^{13} \text{ m/m}^3$). On the other hand, the 9Cr–2WVTa ferritic/martensitic steel was characterized by complex lath subgrains with a higher dislocation density ($\lesssim 10^{15} \text{ m/m}^3$). The dislocation density was higher ($\approx 10^{15} \text{ m/m}^3$) still in the 17Y3 and 12Y1 ODS steels. Finally, among the three ODS steels, the 12YWT had the highest as-processed dislocation density, which varied slightly from grain to grain ($10^{15} - 10^{16} \text{ m/m}^3$). These differences in the initial microstructures have a profound impact on the evolution of defects and cavities during irradiation.

Figs. 1 and 2 compare the oxide particle dispersions in 12Y1 and 12YWT, respectively. Electron diffraction indicated that most oxide particles in 12Y1 were in crystalline form, the particle sizes ranging from 10 to 40 nm diameter. Particle distribution was non-uniform, with the number density in the range of $10^{20} - 10^{21} \text{ m}^{-3}$. Besides the large particles, numerous tiny particles a few nm in diameter were also present. Although not shown here, the particles in 17Y3 steel were coarser and fewer in number compared with those in 12Y1. By comparison, much finer (median 3–5 nm diameter) and finely

dispersed particle-like objects were found in the 12YWT steel. Surprisingly, however, except for diffraction spots from occasional large particles, neither diffraction spots nor amorphous rings were derived from these small objects. A dark-field image from a matrix diffraction spot revealed profuse white specks, presumably arising from the strain contrast around these objects (Fig. 2), suggesting that these objects may be clusters of atoms which reside as solid solution with lattice mismatch around them. The cluster number density in 12YWT steel was estimated to be in the range $1 - 2 \times 10^{23} \text{ m}^{-3}$ by counting the white strain-contrast specks in the weak-beam dark-field image.

During irradiation, dislocation microstructures were modified and cavities formed. Figs. 3 and 4 are low magnification TEM micrographs for the five steels irradiated to 50 dpa and 260 appm He at 650°C. The microstructure of the irradiated solution annealed AISI 316LN showed bubbles ($r < 0.5 \text{ nm}$), voids ($0.5 \text{ nm} \lesssim r < 100 \text{ nm}$), faulted interstitial loops, and segments of line dislocations. Here, the term ‘bubble’ is used to describe cavities smaller than a certain critical size where a bimodal cavity size distribution is observed, and ‘void’ describes cavities larger than the critical size, which grow via a bias-driven mechanism (by absorption of vacancies without the aid of gas atoms). The definition of the critical cavity size and a theoretical basis for the

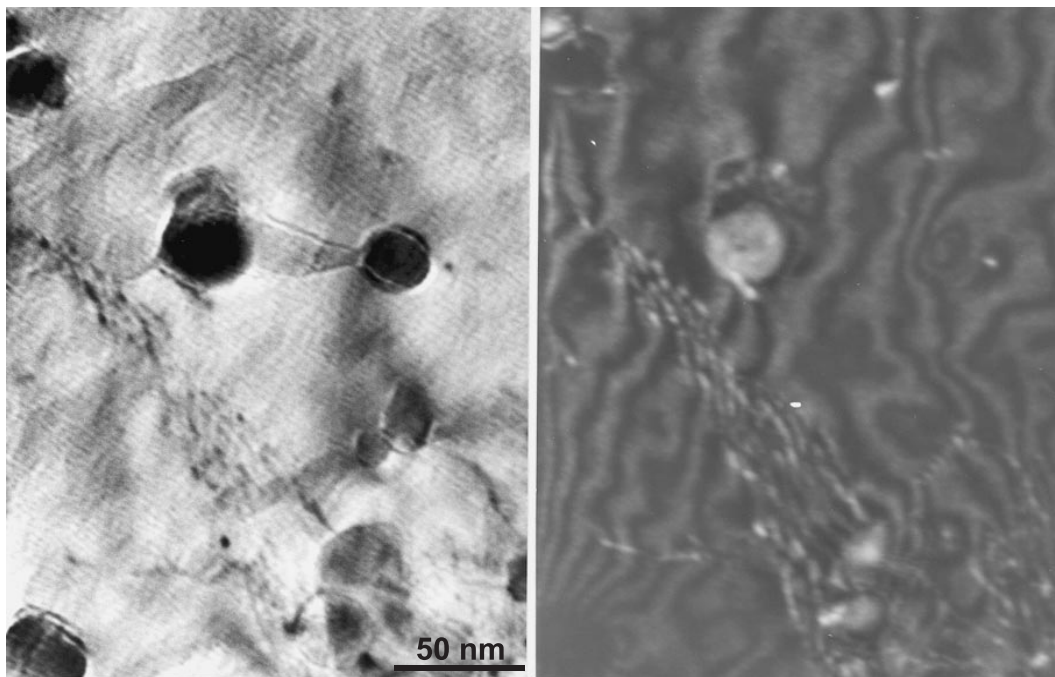


Fig. 1. Microstructure of unirradiated 12Y1 ODS steel: bright- and dark-field TEM micrographs taken near beam direction $B \approx \langle 1\ 2\ 2 \rangle$. The weak-beam dark-field image is taken at $g = 110$, (g , $4g$) diffracting condition. Y_2O_3 precipitate particle sizes are in the range of a few tens of nanometers in diameter.

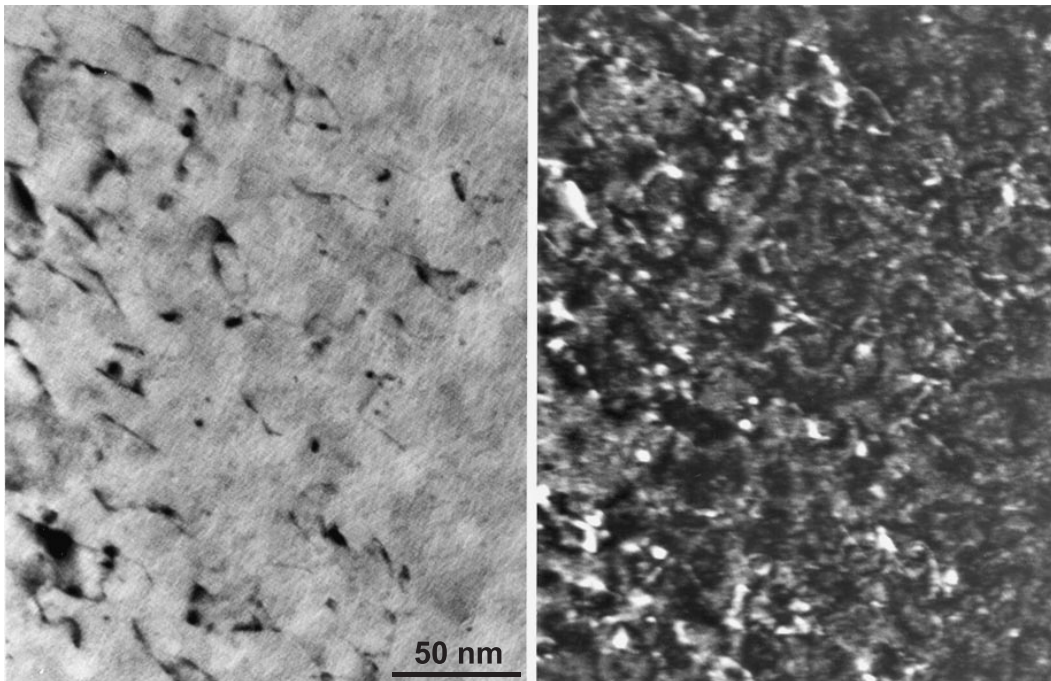


Fig. 2. Microstructure of unirradiated 12YWT ODS steel: bright- and dark-field micrographs taken near beam direction $B \approx \langle 100 \rangle$. The weak-beam dark-field image is taken at $g = 110$, $(g, 4g)$ diffracting condition. The average cluster size is in the range of 3–5 nm. No diffraction spots were seen from these particles, but the presence of high number density clusters is apparent from the strain contrast of clusters in dark-field image.

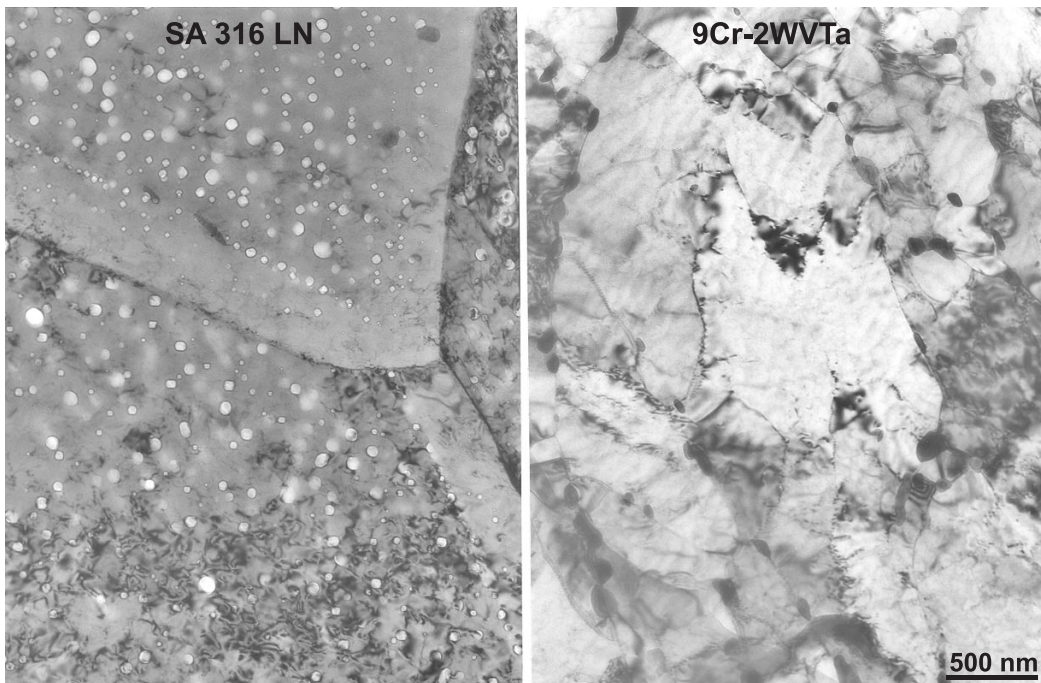


Fig. 3. Low magnification microstructure of solution annealed AISI 316LN austenitic stainless and 9Cr-2WVTa ferritic/martensitic steels after irradiation to 50 dpa (260 appm He) at 650°C with 3.2 MeV Fe^+ and 330 keV He^+ ions.

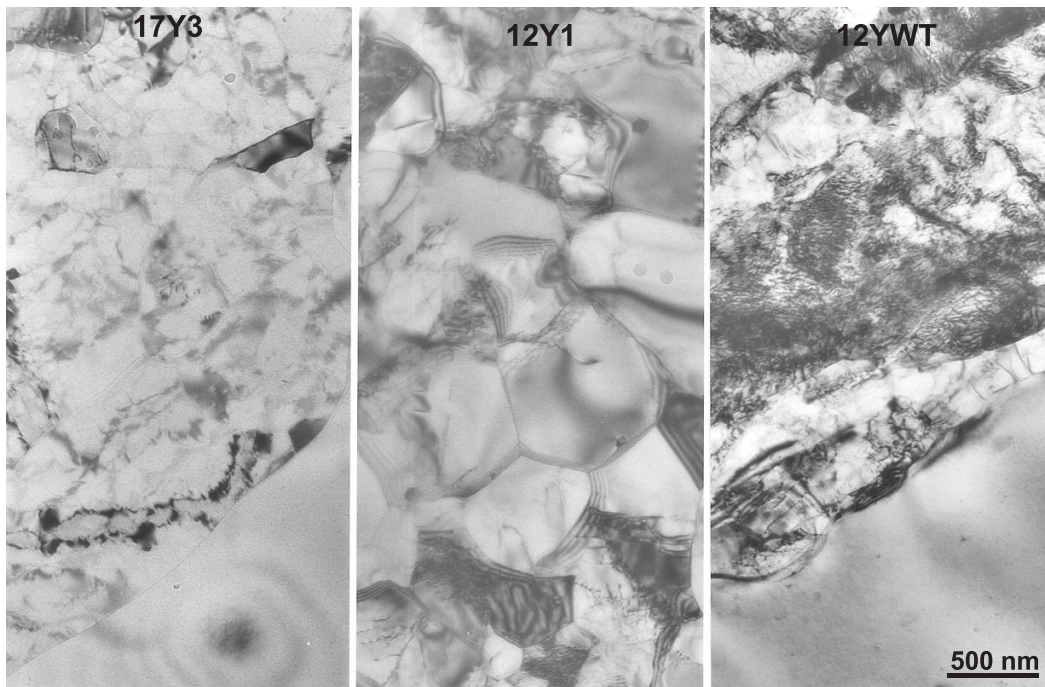


Fig. 4. Low magnification microstructure of 17Y3, 12Y1, and 12YWT ODS ferritic steels after irradiation to 50 dpa (260 appm He) at 650°C with 3.2 MeV Fe⁺ and 330 keV He⁺ ions.

appearance of a bimodal cavity size distribution will be further clarified in Section 4. In the ferritic steel subgrains, varying degrees of dislocation recovery were observed after irradiation, but only a few subgrains showed complete recovery. The least amount of radiation-induced recovery occurred in the 12YWT ODS steel. Although bubbles and voids were not clearly visible at low magnification, high magnification micrographs showed that bubbles and voids were also present in the 9Cr–2WVTa and ODS steels, mainly in the recovered areas.

Figs. 5 and 6 show high magnification microstructures of the irradiated steels corresponding to Figs. 3 and 4. Bimodal cavity size distributions can be seen clearly in the solution annealed AISI 316LN and 9Cr–2WVTa steels in the magnified insets in Fig. 5. In the 9Cr–2WVTa steel, dislocation loops were nucleated in the recovered area, in which bubbles ($r < 0.5$ nm) and voids ($0.5 \text{ nm} \lesssim r < 10$ nm) were also found, mainly associated with the irradiation induced dislocation loops and remnant dislocations. In both the 17Y3 and 12Y1 steels, voids were very small ($r < 5$ nm) but a careful examination clearly indicated bimodal cavity size distributions. The 12YWT steel contained the highest concentration and the finest bubbles ($r < 1$ nm), but there was no indication of bimodal cavity development. Overall, the microstructural evidence indicated that bimodal cavity evolution occurred earliest in the solution

annealed AISI 316LN austenitic stainless steel, next in the 9Cr–2WVTa ferritic/martensitic steel, and last in the 17Y3 and 12Y1 ODS steels.

However, a bimodal cavity distribution did not develop in the 12YWT ODS steel. Although bubbles in the 12YWT were too small to make a precise counting, very high number density of bubbles seems to present in association with dislocations and clusters. It is well known that dislocations and misfit particle interfaces are good gas atom trap sites. Therefore, in consideration of the initial high density of dislocations and the high number of misfit clusters confirmed by APFIM and TEM, the bubble number density in 12YWT is believed to be in the range of 10^{23} – 10^{24} m^{-3} .

4. Discussion

Before discussing the radiation-induced microstructures, the findings on the nature of oxide particles by APFIM and X-ray are reviewed here first to better understand the nature of mechanically alloyed ODS steels.

In an independent APFIM study [20] of the 12YWT steel, (Ti, O, Y, C, B, Cr)-rich nebulous clusters were found to be present, embedded in the matrix of the host Fe, with atomic Y and O scattered around them, rather than as well-defined isolated particles, Fig. 7, confirming the TEM diffraction results. The cluster number density

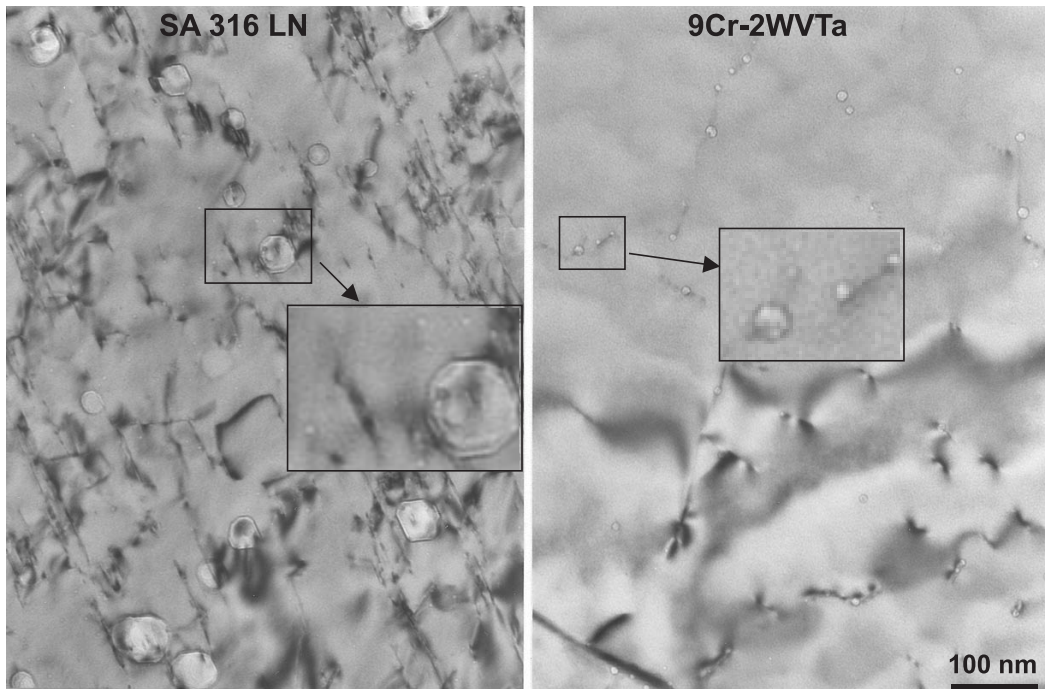


Fig. 5. High magnification microstructure of solution annealed AISI 316LN austenitic stainless and 9Cr-2WVTa ferritic/martensitic steels after irradiation to 50 dpa (260 appm He) at 650°C with 3.2 MeV Fe⁺ and 330 keV He⁺ ions.

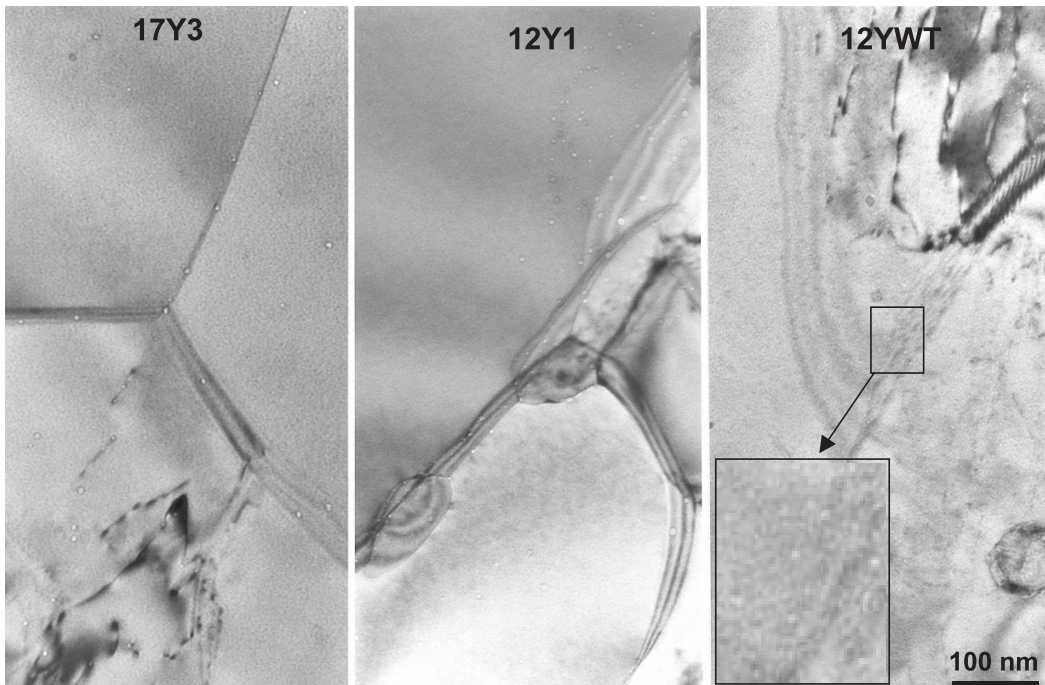


Fig. 6. High magnification microstructure of 17Y3, 12Y1, and 12YWT ODS ferritic steels after irradiation to 50 dpa (260 appm He) at 650°C with 3.2 MeV Fe⁺ and 330 keV He⁺ ions.

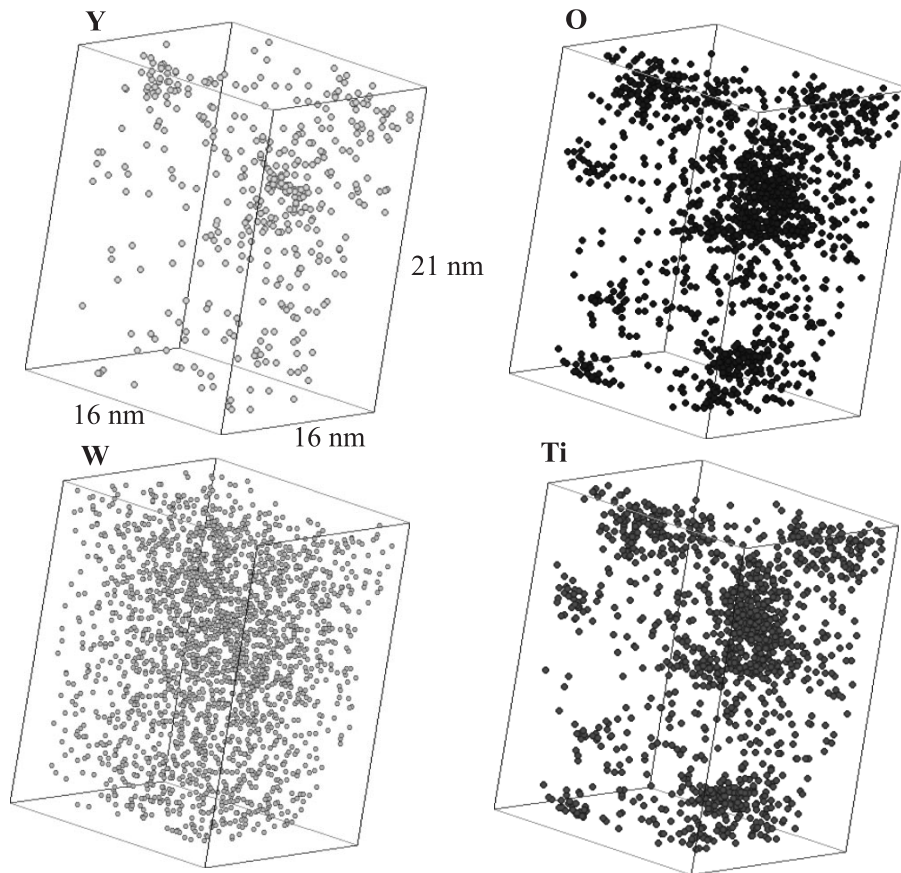


Fig. 7. APFIM image of the oxide clusters in 12YWT ODS steel. The fine (1–7 nm) oxide cluster regions are depleted in Fe and enriched in Y, Ti, O, Cr, C, and B. The composition of the arrow-marked cluster is in at.% $\text{Fe}_{\text{bal}}\text{Cr}_{15.3}\text{W}_{0.70}\text{Y}_{1.21}\text{Ti}_{4.32}\text{O}_{3.78}\text{C}_{0.57}\text{Si}_{0.19}\text{B}_{0.13}$. The scatter of Y and O atoms around the clusters and the enrichment of Ti, C and B in the clusters suggest that the original Y_2O_3 particles were smashed into atomic scale during mechanical alloying and reconstructed as new clusters during the final annealing process at 1050°C. The refinement of particle size occurred only in the presence of Ti.

was estimated to be about $1 \times 10^{24} \text{ m}^{-3}$, an order of magnitude higher than those observed by TEM. In particular, O was found to be in strong association with Ti, seemingly as a single TiO_x complex or a cluster of such. Interestingly, tungsten was distributed uniformly in the matrix showing no particular association with any specific element, but refinement of cluster sizes were observed in ODS steel with W but no Ti added [20]. The sizes of the enriched core were in the range of a few to several nm in diameter, a similar size scale found in TEM.

In 12Y1 steel, no fine clusters were found, but rather large ($\approx 30 \text{ nm}$) and well-defined (Y, O, C)-rich clusters were present in association with scattered Y, O, and C atoms around them, Fig. 8. These results suggest that a substantial fraction of the crushed and smeared particles during MA recrystallized into a larger cluster by accommodating other alloying elements in the matrix

during the final annealing at 1050°C. This is significantly different from the clustering behavior observed in Ti-added 12YWT steel, indicating that Ti might have a significant role in the refinement of oxide particles during annealing. Finally, it should be noted that thermally produced precipitates such as M_{23}C_6 and MC appear as well-defined isolated particles in APFIM.

In X-ray diffraction analyses, it was found that Y_2O_3 particles broke down into smaller sizes with increasing MA time, eventually below the detection limit after 48 h of milling in various ODS steels [21]. X-ray diffraction analyses of the mechanically alloyed Ti-containing ODS steel showed the characteristic b.c.c. iron matrix peaks but no Y_2O_3 peaks, suggesting that Y_2O_3 dissociated into atomic yttrium and oxygen during the MA process, eventually producing a single phase solid solution. Very weak new peaks corresponding to Y_2O_3 , Y_2TiO_5 ($\text{Y}_2\text{O}_3 + \text{TiO}_2$), and $\text{Y}_2\text{Ti}_2\text{O}_7$ ($\text{Y}_2\text{O}_3 + 2\text{TiO}_2$) began to

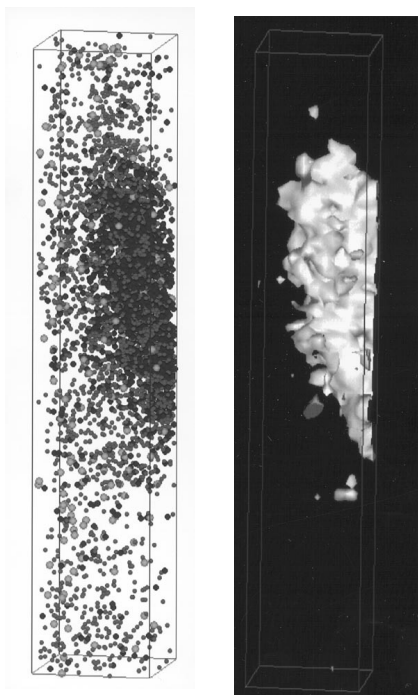


Fig. 8. APFIM image of the oxide particles in 12Y1 ODS steel. Shown here is an oxide particle in a ($10 \times 10 \times 50 \text{ nm}^3$) box: light dots – Yttrium ($\sim 1\%$), medium dots – Carbon ($\sim 5\%$) and dark dots – Oxygen ($\sim 10\%$). The white particle on the right is the contour of $5\% \text{ Y} + \text{O} + \text{C}$ surface. Dispersion of constituent elements of Y_2O_3 is evident around the particle suggesting that atomization of Y_2O_3 particle also occurred during mechanical alloying. The particles are enriched in Y, O and C, much different from that of original Y_2O_3 , again suggesting that the clustering (recrystallization in this case) occurred during the secondary annealing process. These particles are found to be in crystalline form under TEM. Particle sizes in ODS steels without Ti were larger than those in ODS steel with added Ti.

emerge after annealing at 1000°C for 1 h, but no new peaks were observed for 900°C annealing. The Y_2O_3 peak after 1000°C annealing was very small and broad,

indicating either a smaller fraction or a finer dispersion of the dissociated Y_2O_3 recrystallized at this temperature. The intensity of the new peaks increased with increasing annealing temperature, becoming prominent above 1200°C . Most particle sizes were initially smaller than 1 nm, smaller even than the unit cell dimension of cubic Y_2O_3 (1.06 nm), indicating that Y_2O_3 particles were almost atomized during MA. Electron diffraction and X-ray analyses of the extracted particles from the 1100°C annealed ODS steels also indicated that Y_2O_3 particles were in the form of fine ($\approx 3 \text{ nm}$) Y_2TiO_5 and $\text{Y}_2\text{Ti}_2\text{O}_7$ complex clusters in the presence of Ti, whereas crystalline coarse ($\approx 13 \text{ nm}$) Y_2O_3 and Y_2SiO_5 particles were present in 12Cr– Y_2O_3 steel with no added Ti [22], consistent with the new APFIM findings.

The microstructures of irradiated austenitic stainless, ferritic/martensitic, and ODS ferritic steels were examined after a displacement damage of 50 dpa and 260 appm helium implantation at 650°C with 3.2 MeV Fe^+ and 330 keV He^+ ions. The results showed that void formation in the irradiated steels diminished with increasing complexity of the initial microstructure as summarized in Table 2.

The most conspicuous void formation occurred in solution annealed AISI 316LN austenitic stainless steel with the lowest dislocation density, then 9Cr–2WVTa ferritic/martensitic steel with more dislocations, then the 17Y3 ODS steel with the coarser oxide dispersions and higher dislocation density, then 12Y1 ODS steel, and finally only bubbles were present in 12YWT ODS steel with the finest oxide cluster dispersions and the highest dislocation density. The development of a bimodal cavity size distribution occurred in all but the 12YWT. Void formation in the AISI 316LN was accompanied by the formation of interstitial faulted loops followed by the development of prismatic loops and line dislocations, and void formation in ferritic steels occurred mainly in the recovered areas in the subgrains. The most refined bubble distribution and the least dislocation recovery were found in the 12YWT steel, which contained the finest oxide dispersion.

Table 2
Summary of microstructure before and after irradiation

Steels	Before irradiation	After irradiation
SA AISI 316LN	Well-defined clean grains low dislocation density, $\rho_l \ll 10^{13} \text{ m/m}^3$	Evolution of black dots, faulted loops, prismatic loops, line dislocations, and bimodal cavities ($< 100 \text{ nm}$ radius)
9Cr–2WVTa	Complex lath subgrains, $\rho_l \lesssim 10^{15} \text{ m/m}^3$	Partial recovery of dislocations bimodal cavities ($< 10 \text{ nm}$ radius)
17Y3	Finer complex subgrains with coarse and fine particles, $\rho_l \approx 10^{15} \text{ m/m}^3$	Partial recovery of dislocations bimodal cavities ($< 5 \text{ nm}$ radius)
12Y1	Finer complex subgrains with coarse and fine particles, $\rho_l \approx 10^{15} \text{ m/m}^3$	Partial recovery of dislocations bimodal cavities ($< 5 \text{ nm}$ radius)
12YWT	Finest complex subgrains with finest particles or clusters, $\rho_l = 10^{15} - 10^{16} \text{ m/m}^3$	Partial recovery of dislocations unimodal bubbles ($< 1 \text{ nm}$ radius)

Generally, void formation in ferritic/martensitic steel is delayed compared to that in solution annealed 300 series austenitic stainless steel under the same irradiation condition. However, this difference in void formation between the two different types of steels is not considered to stem from fundamental differences in material parameters (i.e., crystal structure, point defect diffusivity, migration energy, formation energy, etc.). Rather, the apparent void formation resistance of the ferritic/martensitic steels originates from the difference in microstructure, namely high density dislocations in the subgrains in the ferritic/martensitic structure. It has been well documented that void formation was also suppressed in austenitic stainless steel when a high density of dislocations were introduced by cold working, and/or the microstructure contained a high number density of precipitates and/or He-bubbles [14,23].

During irradiation, bubbles nucleate and grow by forming vacancy–gas-atom complexes as they accumulate gas atoms. When bubbles exceed a certain critical size or accumulate a certain number of gas atoms, they can grow inexorably by absorbing vacancies without the need for gas atoms. This process is often referred to as a ‘bias-driven mechanism.’ When bubbles are smaller than a certain size, thermal emission prevails over the absorption of vacancies. This demarcates bubble sizes below and above the critical size, which causes development of a bimodal cavity size distribution. Numerous examples of bimodal cavity distributions are documented in [24]. Here, cavities below the critical size are simply called ‘bubbles,’ and the larger ones ‘voids.’ A more rigorous definition of the critical cavity and the related theoretical concepts can be found in [25–27].

The critical cavity size is not a fixed number, but varies dynamically with material parameters, irradiation conditions, and microstructure. Specifically, vacancy supersaturation, and correspondingly void formation, are affected by material parameters, temperature, defect and gas generation rates, and sink number density (dislocations, precipitates, cavities). In the presence of a high number of sinks, most of the interstitials and vacancies produced by radiation recombine at the sinks and fewer vacancies are available for cavity growth. This causes the critical cavity size to increase, and void formation becomes more difficult. In the absence of sinks, most point defects recombine in the matrix and the same effect on void formation results. Dislocation bias (preferential absorption for interstitials over vacancies or vice versa) is not a fixed value either, and it also varies with the state of dislocation evolution. Tangled or pinned (by particles or bubbles) dislocations are difficult to climb up or down, and this makes the bias in a high dislocation density microstructure initially very low, particularly for dislocations immobilized by pinning. Pinned dislocations not only have a low bias, but also have difficulty

recovering, as observed in the 12YWT ODS steel. Precipitate–matrix interfaces are particularly good trap sites for gas atoms, and thus very fine dense precipitates lead to a microstructure with a high concentration of fine bubbles. In such a system, the available helium atoms are diluted over many bubbles as the bubbles themselves also act as recombination sites. In effect, such feedback makes the critical cavity size large, which requires more helium for conversion from bubbles to voids.

Critical quantities associated with cavity formation are calculated by employing the rate theory formulation described in [14]. The results of the calculations are shown in Fig. 9. The calculations require detailed knowledge of material parameters, irradiation variables, and microstructural information. The material parameters used in the calculation are summarized in the figure caption. Although precise material parameters are still unknown, the material parameters used here have been justified previously. Moreover, the outcomes of the calculated values are determined most sensitively by the dominant sink strength (dislocation density and cavity number density), and the use of a wide range of material parameter values does not greatly alter the calculations. In the irradiated ODS steels, the cavity sizes were too small to derive microstructural statistics from the TEM micrographs. So, the microstructural data used for calculations are approximate and the results are qualitative. However, they do clearly show that there exists a fundamental physical basis to explain the development of a bimodal cavity distribution, its delay, or perhaps near indefinite delay in systems with very high number density of fine precipitates, such as the oxide clusters found in the 12YWT steel.

In Fig. 9, the variations of critical cavity radius are plotted as a function of dislocation density for two different cavity number densities and dislocation biases with the corresponding helium concentration levels on the right. The helium concentration that is required for all cavities to reach a critical size ($N_g^* \times N_c$, number of helium atoms per critical cavity multiplied by the cavity number density) is expressed in appm.

The implications of the plots are the following: (1) in a solution annealed or low dislocation system, the critical cavity radius (r_c^*) is initially large because most point defects recombine in the matrix. r_c^* decreases as dislocation microstructure evolves (i.e., black dots faulted interstitial loops \rightarrow unfaulted prismatic loops \rightarrow line dislocations); (2) in a cold worked (CW) system, r_c^* is initially large, this time because most point defects recombine at dislocations and r_c^* decreases as dislocations recover by either climbing up or down by absorbing vacancies or interstitials during irradiation; (3) when the cavity number density is high, cavities themselves become the point defect recombination sites and r_c^* becomes large, particularly in the low dislocation density regime; (4) when dislocation bias decreases (i.e., by

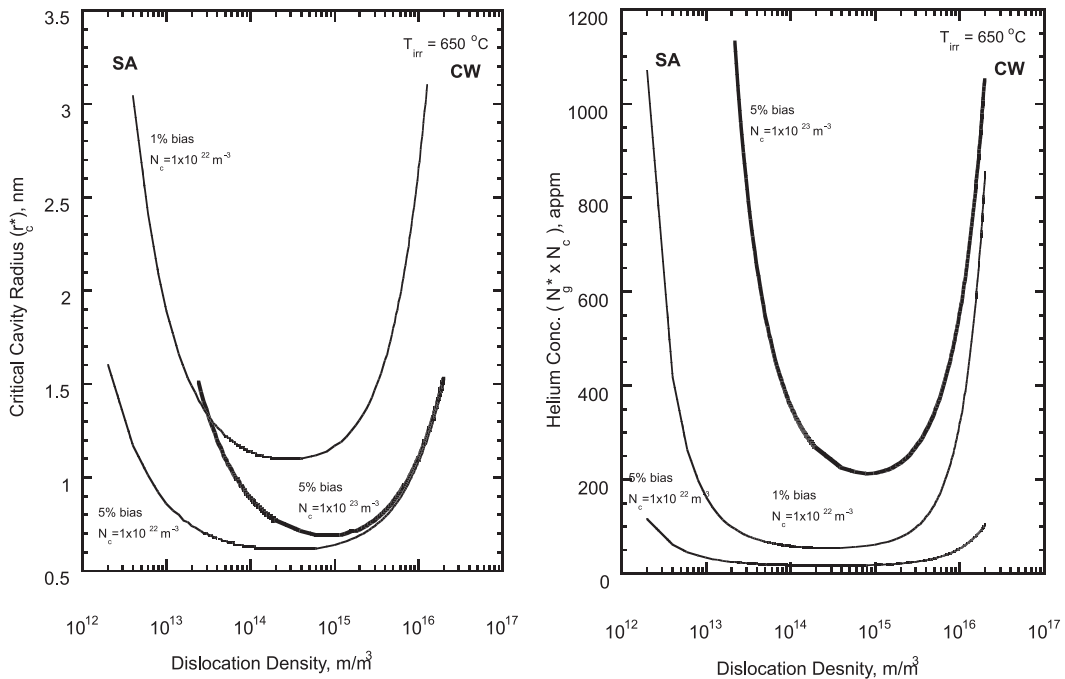


Fig. 9. Variation of critical cavity radius as a function of dislocation density and the corresponding helium concentration ($N_g^* \times N_c$, number of helium atoms per critical cavity multiplied by the cavity number density). The plots are made for two different cavity number densities and dislocation biases. The parameters used in this computation are displacement damage rate $G = 1 \times 10^{-3}$ dpa/s, vacancy diffusivity pre-exponential $D_v^0 = 1 \times 10^{-6}$ m²/s, interstitial diffusivity pre-exponential $D_i^0 = 1 \times 10^{-6}$ m²/s, vacancy migration energy $E_v^m = 1.2$ eV, interstitial migration energy $E_i^m = 0.15$ eV, vacancy formation energy $E_v^f = 1.6$ eV, vacancy formation entropy $S_v^f = 1.29 \times 10^{-4}$ eV/K, and surface energy $\gamma = 1.5$ J/m². Dislocation bias changes with microstructural evolution and thus precise bias values are not known. For simulation, 1% and 5% bias values were used.

pinning dislocations), defect recombination is enhanced and r_c^* becomes large; (5) finally, when the cavity number density increases (i.e., by introducing a high number of gas atom trap sites such as fine particles in the ODS steel), r_c^* increases and the helium required for the onset of bias-driven cavity growth increases for the reasons mentioned already.

From the above considerations it can be said that: (1) solution annealed AISI 316LN austenitic stainless steel, defect evolution was rapid and bias-driven void growth started earlier; (2) the 9Cr–2WVTa ferritic/martensitic steel, bias-driven void growth was delayed because of the initial high density of dislocations and slow recovery; (3) the 17Y3 and 12Y1 ODS steels, bias-driven void growth was further delayed because of slow recovery and a low dislocation bias due to oxide particle pinning; (4) in the 12YWT ODS steel, the latter effects were further amplified by the presence of a very high number density of fine oxide clusters. While microstructural evolution can be studied in more detail as a function of dose or the bias change in association with precipitate pinning, overall response of the materials to irradiation is generally in accord with theoretical expectations.

5. Conclusions

Void formation mechanisms in solution annealed AISI 316LN austenitic stainless steel, 9Cr–2WVTa ferritic/martensitic steel, and three (17Y3, 12Y1 12YWT) ODS ferritic steels were examined after irradiation to 50 dpa with 260 appm simultaneous helium injection at 650°C with 3.2 MeV Fe⁺ and 330 keV He⁺ ions. These results showed that void growth was delayed with increasing microstructural complexity, namely by increasing the dislocation density and immobilizing dislocations via nanoscale oxide particles and clusters. The most significant void suppression occurred in 12YWT ODS steel, which possessed the highest dislocation density and the finest and highest number of oxide clusters. Analyses based on a rate theory model suggested that the sink density in the system dictates point defect recombination and void formation, and that change in bias could also be a significant factor in controlling void formation and growth. The suppression of void formation in the ODS steels is attributable to the initial high density of dislocations, slow dislocation recovery by oxide particle pinning, low bias of immobilized or pinned dislocations, and to the nucleation of a

high number density of cavities by trapping helium atoms at particle–matrix interfaces. Overall the data suggest that, within a practical limit, void formation can be suppressed if the dislocation microstructure is stabilized and helium bubbles are dispersed on a fine scale via fine stable oxide particles or atom clusters. However, for steel with such a microstructure, radiation hardening-induced embrittlement could become a concern. Further research is clearly needed prior to the application of ODS steels for fission and fusion structural materials.

Acknowledgements

This research was sponsored in part by the Division of Materials Sciences, US Department of Energy under contract No. DE-AC05-00OR22725 and in part by the Office of Fusion Energy, US Department of Energy, under contract No. W-7405-eng-26 with UT-Battelle, LLC. One of the authors, Kim, thanks ORNL for the support during his graduate research. The authors thank Drs Kleuh and Rowcliffe for technical review of the manuscript.

References

- [1] S. Ukai, T. Nishida, H. Okuda, M. Inoue, M. Fujiwara, T. Okuda, K. Asabe, in: Proceedings of the International Symposium on Materials Chemistry in Nuclear Environment, Materials Chemistry'96, Tsukuba, Ibaraki, Japan, 14–15 March 1996, p. 891.
- [2] S. Ukai, T. Nishida, H. Okada, T. Okuda, M. Fujiwara, K. Asabe, *J. Nucl. Sci. Technol.* 34 (1997) 256.
- [3] D.K. Mukhopadhyay, F.H. Froes, D.S. Gelles, *J. Nucl. Mater.* 258–263 (1998) 1209.
- [4] T. Okuda, S. Nomura, M. Nakanishi, M. Fujiwara, H. Takahashi, in: Proceedings of the First Japan International SAMPE Symposium, 28 November–1 December 1989, p. 1616.
- [5] J. Ohta, T. Ohmura, K. Kako, M. Tokiwai, T. Suzuki, *J. Nucl. Mater.* 225 (1995) 187.
- [6] D.S. Gelles, in: F.A. Garner, N.H. Packan, A.S. Kumar (Eds.), Proceedings of the 13th International Symposium (Part I), ASTM STP 995, ASTM, Philadelphia, PA, 1987, p. 560.
- [7] E.A. Little, D.A. Stow, *Mater. Sci.* (March) (1980) 89.
- [8] J.M. Vitek, R.L. Klueh, *J. Nucl. Mater.* 122&123 (1984) 245.
- [9] Ulrich Stamm, H. Schroeder, *J. Nucl. Mater.* 155–157 (1988) 1059.
- [10] J.J. Kai, R.L. Klueh, *J. Nucl. Mater.* 230 (1996) 116.
- [11] L.L. Horton, L.K. Mansur, in: F.A. Garner, J.S. Perrin (Eds.), Proceedings of the 12th International Symposium, ASTM STP 870, ASTM, Philadelphia, PA, 1985, p. 344.
- [12] K. Farrell, E.H. Lee, in: F.A. Garner, J.S. Perrin (Eds.), Proceedings of the 12th International Symposium, ASTM STP 870, ASTM, Philadelphia, PA, 1985, p. 383.
- [13] L.K. Mansur, *J. Nucl. Mater.* 206 (1993) 306.
- [14] E.H. Lee, L.K. Mansur, *Metall. Trans. A* 21 (1990) 1021.
- [15] L.K. Mansur, E.H. Lee, *J. Nucl. Mater.* 179–181 (1991) 105.
- [16] T. Okuda, S. Nomura, S. Shikakura, K. Asabe, S. Tanoue, M. Fujiwara, in: A.H. Clauer, J.J. deBarbadillo (Eds.), Minerals, Metals and Materials Society, TMS, USA, 1990, p. 195.
- [17] M.B. Lewis, W.R. Allen, R.A. Buhl, N.H. Packan, S.W. Cook, L.K. Mansur, *Nucl. Instrum. and Meth. B* 43 (1989) 243.
- [18] J.F. Ziegler, J.P. Biersack, U. Littmark, *The Stopping and Range of Ions in Solids*, Pergamon, Oxford, 1985.
- [19] E.H. Lee, *Nucl. Instrum. and Meth. B* 151 (1999) 29.
- [20] D.J. Larson, P.J. Maziasz, I.-S. Kim, K. Miyahara, Three dimensional atom probe observation of nanoscale titanium–oxygen clustering in an oxide-dispersion-strengthened Fe–12Cr–3W–0.4Ti + Y₂O₃ ferritic alloy, *Scripta Mater.* (submitted).
- [21] T. Okuda, M. Fujiwara, *J. Mater. Sci. Lett.* 14 (1995) 1600.
- [22] S. Nomura, T. Okuda, S. Shikakura, M. Fujiwara, K. Asabe, in: A.H. Clauer, J.J. deBarbadillo (Eds.), Minerals, Metals and Materials Society, TMS, USA, 1990, p. 203.
- [23] E.H. Lee, L.K. Mansur, *Metall. Trans. A* 23 (1992) 1977.
- [24] L.K. Mansur, E.H. Lee, P.J. Maziasz, A.F. Rowcliffe, *J. Nucl. Mater.* 141–143 (1986) 633.
- [25] L.K. Mansur, *Nucl. Technol.* 40 (1978) 5.
- [26] L.K. Mansur, in: G.R. Freeman (Ed.), *Kinetics of Non-homogeneous Process*, Wiley, 1989, p. 377 (Chapter 8).
- [27] L.K. Mansur, W.A. Coghlan, *J. Nucl. Mater.* 119 (1983) 1.